International Journal of Applied Earth Observations and Geoinformation 110 (2022) 102827

Contents lists available at ScienceDirect

International Journal of Applied Earth Observations and Geoinformation

journal homepage: www.elsevier.com/locate/jag

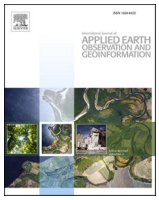

Downscaling MODIS nighttime land surface temperatures in urban areas using ASTER thermal data through local linear forest

Cheolhee Yoo [a,b], Jungho Im [a,*], Dongjin Cho [a], Yeonsu Lee [a], Dukwon Bae [a], Panagiotis Sismanidis [c]

[a] Department of Urban and Environmental Engineering, Ulsan National Institute of Science and Technology (UNIST), Ulsan, South Korea
[b] Department of Land Surveying and Geo-Informatics, The Hong Kong Polytechnic University, Hung Hom, Kowloon, Hong Kong
[c] Institute of Geography, Ruhr University Bochum, Bochum, Germany

ARTICLE INFO

Keywords:
Downscaling
Thermal remote sensing
Land surface temperature (LST)
Local linear forest
MODIS
ASTER

ABSTRACT

Spatial downscaling effectively produces high spatiotemporal resolution land surface temperature (LST) in urban areas. Although nighttime LST is an essential indicator in urban thermal research, few LST downscaling studies have focused on nighttime in fine resolution. This study proposed a novel approach using local linear forest (LLF) to downscale 1 km Moderate Resolution Imaging Spectroradiometer (MODIS) nighttime LSTs to 250 m spatial resolution in three cities: Rome, Madrid, and Seoul. First, we used Least Absolute Shrinkage and Selection Operator (LASSO) to select a set of past clear-sky ASTER LSTs (ALST) which showed a high spatial correlation with the target MODIS LST. Downscaling models were then developed using input kernels of the selected ALSTs and eight auxiliary variables: normalized difference vegetation index (NDVI), elevation, slope, built-up area percentage, road density, population density, wind speed, and distance from the built-up weighted center of the study area. Three schemes were evaluated: scheme 1 (S1) using only auxiliary variables as input kernels with a random forest (RF) model; scheme 2 (S2) using selected ALSTs and auxiliary variables as input kernels with an RF model; and scheme 3 (S3) using input kernels as in S2 but with the LLF model. Validation was performed using bias-corrected ALSTs for seven reference dates in the three cities. LLF-based S3 showed the highest accuracy with an average correlation coefficient (R) ~ 0.94 and Root Mean Square Error (RMSE) ~ 0.64 K while maintaining the dynamic range of the original LST at the finer resolution. The downscaled LST (DLST) based on S3 effectively depicted the nocturnal thermal spatial pattern in greater detail than the other two schemes did. The S3-based DLST also showed a relatively high spatial correlation with the *in-situ* nighttime air temperature within the cities. When compared to the original 1 km LST, S3-based DLST showed larger surface urban heat island intensity for the urban-type surfaces and a higher temporal correlation with nighttime air temperature.

1. Introduction

Due to the rapid population increase and city development, natural ground covers such as forests and bare soils have been replaced by impervious surfaces (Yuan and Bauer, 2007). High solar absorption and large thermal capacity and conductivity of pavements, buildings and other impermeable surfaces make the compact urban cores warmer than the surrounding areas. This is referred to as the urban heat island (UHI) effect, and its magnitude varies by the structure, density, and material of the urban surface (Stewart and Oke, 2012). Moreover, the heat absorbed during the daytime is released through the night at different rates for various surface types, resulting in different spatial patterns of temperature during the day and night in cities (Azevedo et al., 2016).

One of the most important data sources for urban climate monitoring is Land Surface Temperature (LST), retrieved from satellite thermal infrared sensors. Thanks to its relatively high continuity in the spatio-temporal domain, LST is crucial in analyzing surface UHI (SUHI), investigating urban expansion and measuring heat stress in the cities (Weng et al., 2019; Zhao et al., 2020; Xian et al., 2021). Unfortunately, there is a well-known limitation in the active use of satellite LST in urban areas: the trade-off between temporal and spatial resolution. Moderate Resolution Imaging Spectroradiometer (MODIS) LST from Aqua and Terra satellites has been extensively used for urban climate studies due to its high temporal resolution (i.e., four times a day) with global coverage (Bechtel et al., 2019). However, it is difficult to see the thermal distribution in detail over urban areas using MODIS LST due to its coarse

* Corresponding author.

https://doi.org/10.1016/j.jag.2022.102827
Received 13 March 2022; Received in revised form 15 May 2022; Accepted 16 May 2022
Available online 21 May 2022

spatial resolution (1 km). Recently, Landsat 8 LST with 100 m spatial resolution has been available as level-2 products. However, Landsat has a long revisit cycle (16 days) and the products are mostly available during the daytime. Landsat provided a small number of nighttime LST data only for specific regions. Onboard Terra, the Advanced Spaceborne Thermal Emission and Reflection Radiometer (ASTER) generates LST with a high spatial resolution of 90 m. In particular, ASTER LST has been produced both daytime and nighttime globally for long-term periods (i.e., March 2000 to present). However, ASTER has a low temporal resolution of more than 16 days and a relatively narrow swath width (60 km) so it is not easy to timely obtain LST that fully covers a region of interest at the same time.

Downscaling techniques that improve the spatial resolution of the relatively coarse original data have been widely used to overcome the resolution trade-off between a single satellite sensor's temporal and spatial scales. Various satellite-based products such as soil moisture and precipitation, as well as LST, have been produced at fine scale using downscaling techniques (Peng et al., 2017; Zhao et al., 2021; Abdollahipour et al., 2022). Especially for the LST in urban areas, the kernel-driven method has been most effectively used among various downscaling approaches (Yoo et al., 2020a). The kernel-driven method uses fine-resolution input variables called kernels. The kernels are aggregated to the resolution of a coarse LST, and a relationship between the kernels and the coarse-resolution LST is modeled. Putting the original fine-resolution kernels into this model can generate a fine-resolution LST. In the kernel-driven method, the selection of meaningful kernels is very important. The widely used kernels in LST downscaling are satellite spectral reflectance data and reflectance-based indices such as the normalized difference vegetation index (NDVI), normalized difference water index (NDWI), and normalized difference built-up index (NDBI) (Yang et al., 2017; Pan et al., 2018). Many studies have employed reflectance-based kernels collected concurrently with the target LST (Luo et al., 2021; Yang et al., 2019; Ebrahimy and Azadbakht, 2019). Other frequently used kernels include the digital elevation model (DEM) and the variables derived from DEM, such as slope, due to their high correlation with LST (Bartkowiak et al., 2019). To model the relationship between input kernels and the target LST, various linear-based techniques have been used, including linear regression, ridge regression, and geographically weighted regression (Peng et al., 2019; Duan and Li, 2016). Some kernels, however, tend to have a nonlinear relationship with the target LST, especially on heterogeneous surfaces (e.g., urban areas).

In recent years, machine-learning techniques have been used in LST downscaling over complex study regions (Li et al., 2019; Ebrahimy and Azadbakht, 2019). In particular, tree-based models such as random forest (RF) and extreme gradient boosting (XGBoost) usually have shown better downscaling performance than other machine learning regressors (Li et al., 2019; Sismanidis et al., 2021). However, the widely used tree-based models have a narrow prediction range near the dense distribution of the training samples to minimize the total prediction error (Liu et al., 2020). In fact, fine-resolution LST generally exhibits a larger temperature range than coarse-resolution LST. Unfortunately, the tree-based models cannot extrapolate the outer bounds of the range of the training data of coarse-resolution LST (Li et al., 2019).

Nighttime LST is as important as daytime LST for understanding urban climatology. However, only a few studies have tried to downscale nighttime LST for urban areas to fine resolution (i.e., less than 1 km) based on the kernel-driven method (Wang et al., 2020a; Wang et al., 2020b; Qi et al., 2020). They used the reflectance kernels obtained in the daytime, which do not directly affect the nighttime LST. In other words, the kernels which strongly represent nocturnal thermal properties were absent in the previous studies.

This study attempts to downscale MODIS nighttime LSTs to 250 m spatial resolution in three mega-urban areas: Rome, Madrid, and Seoul. The proposed approach uses ASTER nighttime thermal data and auxiliary variables representing nocturnal thermal characteristics in urban areas as input kernels for downscaling. A new tree-based machine-learning technique called local linear forest (LLF), which leverages the strengths of RF and local linear regression, was applied to model the dynamic range of LSTs effectively. The objectives of this study are to 1) propose a novel nighttime LST downscaling approach using LLF, 2) evaluate the generalization of the proposed models from both quantitative and qualitative aspects, and 3) explore the potential use of the downscaled LSTs for urban climate characterization such as SUHI analysis and air temperature monitoring.

2. Study area and data

2.1. Study area

Rome, Madrid, and Seoul were chosen as the study areas. Rome, the capital city of Italy, is situated in the Italian Peninsula's midwestern region. With 2.9 million citizens living on 1285 km^2, Rome is the most densely populated city in Italy. Rome shows a Mediterranean climate with dry summers and humid winters. The city's urban structure is monocentric, with buildings that are densely concentrated in the city center.

Madrid, the capital of Spain, is a highly populated metropolis in the Iberian Peninsula. Madrid has an inland Mediterranean climate that is bounded on the east by a semi-arid climate. Madrid is Spain's largest city, with 3.2 million people residing in a 604 km^2 territory. The city encompasses the primary metropolitan region, consisting of a monocentric city core and independent municipalities that surround it.

Seoul is the capital of South Korea, which is in the mid-western part of the Korean Peninsula. The Han River runs through the heart of the city, which is bordered by eight mountains. Seoul has a hot-summer humid continental climate. Seoul is a very populated city with 9.7 million residents living in an area of 605 km^2. Rapid urbanization since the 1980s has resulted in a high density of various types of buildings throughout the city. The three megacities are well-suited to evaluating the robustness of the proposed methodology since they reflect various geographic characteristics and unique urban architectures. The study boundaries were determined by covering the core central and surrounding areas of each city (Fig. 1).

2.2. Satellite LST data

MODIS Terra nighttime LST with 1 km spatial resolution was used as the target variable for downscaling. MODIS LST is produced based on a generalized split-window algorithm (Wan and Dozier, 1996). Terra nighttime LST products from 2017 to 2020 for the three study areas (h17v04 for Madrid, h18v04 for Rome, and h28v05 for Seoul) were obtained from MOD11A1 Version 6 downloaded from NASA's Earthdata Search (https://search.earthdata.nasa.gov). The nominal acquisition time of Terra nighttime LST is the local solar time of 10:30p.m. The root mean squared error (RMSE) of MODIS terra nighttime LSTs is less than 2 K in most validation sites over the world (Duan et al., 2019).

This study used ASTER nighttime LST (ALST) as the fine-resolution LST data. The Terra satellite's ASTER thermal infrared (TIR) sensor delivers data in five bands between 8 and 12 μm spectral range, with a spatial resolution of 90 m. ALST has obtained from the ASTER level 2 surface kinetic temperature product (AST_08), provided by NASA's Earthdata Search (https://search.earthdata.nasa.gov). This product is retrieved from the five TIR bands through Planck's Law, which uses emissivity values based on the Temperature-Emissivity Separation (TES) algorithm, with an error of less than 1.5 K (Gillespie et al., 1998). ASTER LST has been used to validate MODIS LST, and the bias between the two products is shown to be relatively low (0.2–1.5 K; Duan et al., 2017). The average local acquisition time for ALSTs was about 10:30p.m. for Rome and Seoul and about 11:00p.m. for Madrid. All available clear-sky ALSTs for each city from March 2000 to May 2021 were obtained. A total of twenty-two ALSTs for Rome, eighteen for Madrid, and five for Seoul

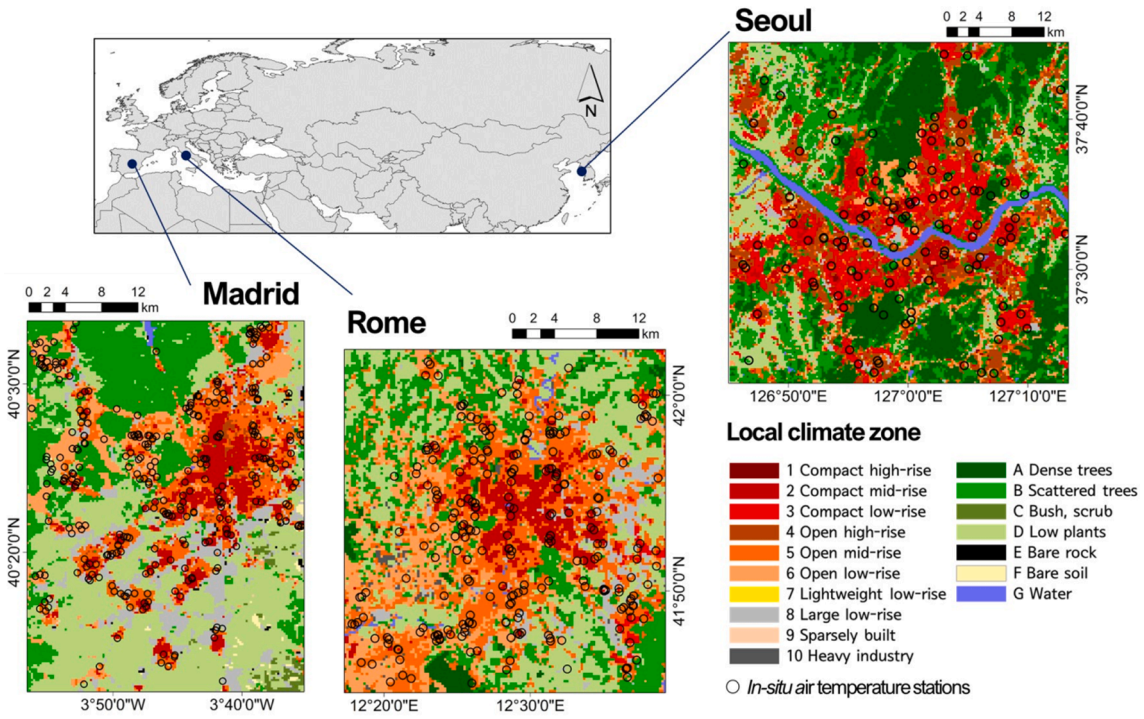

Fig. 1. Study area of three cities. The background layer is the 250 m resolution Local Climate Zone (LCZ). These LCZ maps of three cities were adopted from Yoo et al. (2019) for Rome and Madrid, and Yoo et al. (2020b) for Seoul. The location of *in-situ* weather stations was displayed for each city.

were acquired. The number of ALSTs collected per month is presented in Supplementary Fig. A1.

2.3. Input kernels for LST downscaling

Downscaling the nighttime LST in urban areas requires input kernels that are closely related to the nighttime thermal distribution. This study used ALSTs and eight auxiliary variables as input kernels. Considering the spatial scale of the input kernels, the target spatial resolution of downscaled LST was set to 250 m. It was also confirmed that the variation of nighttime LST was relatively stable within the 250 m grid in the three cities (average standard deviations are in the range of 0.30–0.45 K; See Supplementary Fig. A2).

ALSTs were used as input kernels because these represent nocturnal thermal distribution in fine resolution. All available clear-sky ALSTs with 90 m resolution were mean-aggregated to 250 m. NDVI, which is related to vegetation density, was used as the input kernel. The relationship between NDVI and LST has been used to explain urban surface characteristics (Alexander, 2020). NDVI was produced from reflectance data (i.e., near-infrared (NIR) and red bands) acquired during the daytime. Unfortunately, it is likely to be partially obscured by clouds during the daytime on the same day that clear-sky nighttime LST can be obtained. Therefore, this study used 16-day MODIS NDVI (MOD13Q) with a 250 m resolution, obtained from NASA's Earthdata Search (https://search.earthdata.nasa.gov). For each date, the NDVI with a composite period that included the target date was used as the input kernel. Elevation and slope were chosen as kernels documenting the topographic characteristics of the study area. The effect of solar radiation varies by elevation and slope (Tovar-Pescador et al., 2006). Because the absorbed heat is released during the night, the two variables also indirectly affect the distribution of nighttime LST. The 90 m resolution DEM from the shuttle radar topography mission (SRTM) (https://srtm.csi.cgiar.org) was used to obtain elevation. The 90 m DEM was mean aggregated to 250 m within the target grid area. The slope was calculated from 250 m DEM using the ArcGIS Spatial Analyst. We also used the ten-year average 250 m spatial resolution wind speed (Wind), provided by Global Wind Atlas (https://globalwindatlas.info), as the local climatology kernel. The spatial difference in wind speed affects the LST distribution within the city (Yamamoto and Ishikawa, 2018).

Anthropogenic heat released from energy consumption by human activity increases the nocturnal SUHI magnitude (Liao et al., 2017). Thus, this study also used the 250 m resolution population density (Pop) from the Global Human Settlement population (https://ghsl.jrc.ec.europa.eu/ghs_pop.php) as the input kernel. The amount of impervious surface contributes significantly to nighttime LST distribution in urban areas (Mallick et al., 2013). Two variables representing urban materials—built-up percentage (Built) and road density (Road)—were used as input kernels. The 250 m Built kernel was acquired from the Global Human Settlement built-up grids (https://ghsl.jrc.ec.europa.eu/ghs_bu.php). To construct the Road kernel, line density was calculated from the Open Street Map (https://www.openstreetmap.org) road shapefile to 250 m resolution. In general, cities tend to have higher LST near the city center. By putting the Built as a weight field, the distance from the built-up weighted Center (DisBWC) of the study area was calculated for each 250 m resolution grid.

2.4. LCZ and in-situ air temperature data

To examine the potential for applications of the downscaled LST, Local Climate Zone (LCZ) and *in-situ* air temperatures were obtained for the three cities. LCZ is a universal classification system focusing on urban areas that can be used to characterize the urban thermal climate (Stewart and Oke, 2012). This study used LCZ to analyze the nocturnal SUHI patterns of the three cities. LCZ maps of Rome and Madrid with 100 m spatial resolution were produced from bitemporal Landsat 8 data using a convolutional neural network (CNN) classifier by Yoo et al. (2019). The LCZ map of Seoul with 50 m resolution was produced from multiple data sources, including Sentinel-2A reflectance, Landsat 8 LST, and building datasets based on CNN by Yoo et al. (2020b). All of these LCZs were resampled to 250 m resolution using the majority rule. LCZ consists of ten urban types (LCZ1 to 10) and seven natural types (LCZA to G), and the full LCZ class name is shown in the legend of Fig. 1.

Air temperatures from 2017 to 2020 were gathered from various types of weather stations in three cities after a quality assessment. The nighttime air temperature at 10:30p.m., which is closest to the Terra MODIS nighttime acquisition time, was extracted for the three cities. The distribution of weather stations and the process of the temperature data, including quality checks, are explained in Supplementary B.

3. Methods

3.1. Random forest and local linear forest

This study used two machine learning models for LST downscaling: RF and LLF. RF is a well-known ensemble-based machine learning model for data classification and regression (Breiman, 2001). It comprises multiple independent decision trees (generally more than 500) to avoid overfitting issues through two random processes. RF randomly selects both a subset of samples and features for splitting at a node with allowing duplication (bagging) in a given training set in each decision tree. The final output of RF is calculated by the ensemble mean of all tree results for regression.

RF is regarded as a useful model for many regression tasks thanks to its relatively high performance and low sensitivity to the parameters compared to other techniques (Odebiri et al., 2020; Sahoo et al., 2020). However, RF cannot extrapolate target values outside the range of the training data. Friedberg et al. (2021) recently suggested a new tree-based technique called LLF, which improves the weakness of RF on extrapolation. From an LLF perspective, RF is considered an adaptive kernel method in high dimensions. Specifically, LLF uses the fraction of

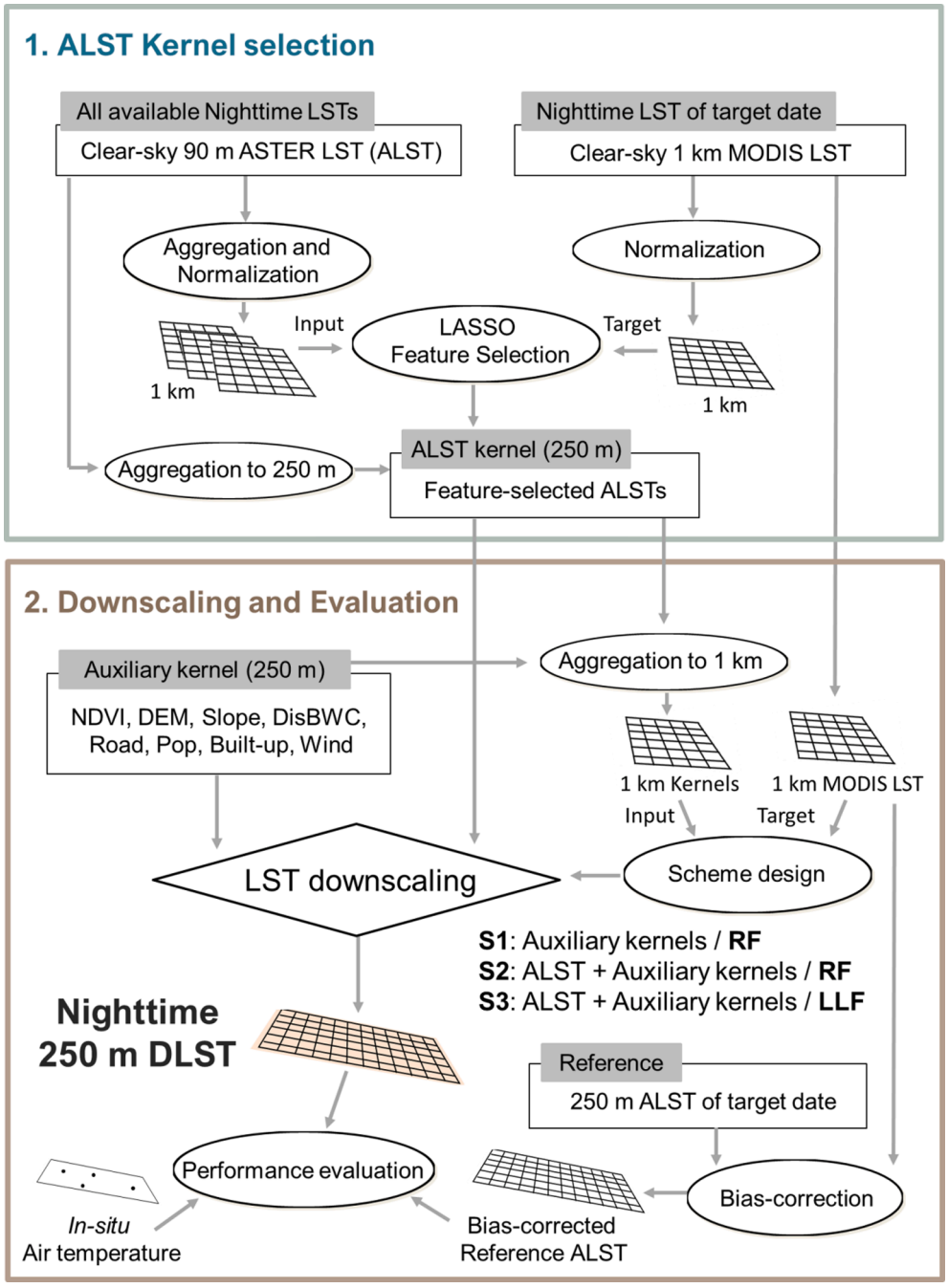

Fig. 2. Flowchart of the LST downscaling approach proposed in this study. The procedures are divided into two sections: ALST kernel selection, and downscaling and evaluation.

trees in which the training sample falls into the same terminal node as the predicted point as the weights to fit a local linear regression. A detailed explanation of LLF is provided in Supplementary C. In this study, The "grf" add-on package (version 2.0.2) was used to implement RF and LLF in R statistical software with default model training parameter settings.

3.2. LST downscaling

The overall procedure for the nighttime LST downscaling consists of two main parts: 1) ALST kernel selection and 2) downscaling and evaluation (Fig. 2). This study assumes that there are nights with a similar spatial distribution of LST among multiple dates, considering there is less solar effect at nighttime. All 250 m resolution ALSTs were mean aggregated to 1 km. Among all available clear-sky ALSTs, we selected those that showed a high spatial correlation with the MODIS nighttime LST of the target date, based on the Least Absolute Shrinkage and Selection Operator (LASSO) (Tibshirani, 1996) feature selection technique (Supplementary D). To select the appropriate ALST kernels for each date, this study applied LASSO to the data for each target date. All 1 km ALSTs were fed into the LASSO as explanatory variables, and the MODIS nighttime LST of each date was used as a response variable.

All input kernels, including the selected ALSTs and eight auxiliary variables, were aggregated to 1 km resolution. Three downscaling schemes were developed based on different input kernels and regression models. The first scheme (S1) uses only auxiliary variables as input kernels in the RF model. The second scheme (S2) uses not only auxiliary variables but also the selected ALSTs together as input kernels in the RF model. Comparison between S1 and S2 allows us to identify the effect of ALSTs as input kernels. The third scheme (S3), which is the main scheme of this study, uses the same input kernels as S2, but the regression model in S3 is LLF. In S3, the selected ALST kernels were used as the linear correction variables in LLF prediction. With S2 and S3, we can compare the downscaling performance of LLF to RF. The models were developed separately for each target date, using 1 km MODIS nighttime LST as target variables. Then, the original fine resolution input kernels of each scheme were fed into the developed models. The 250 m resolution downscaled LSTs (DLST) were finally produced for every target date in each scheme.

Independent ALST and air temperature data were used to evaluate the DLST. Due to the lack of large homogeneous and isothermal sites, *in-situ* LSTs suitable for validating satellite data were rarely available in urban areas. Consequently, the only viable options for evaluating urban DLST are cross-validation with independent satellite data or a "upscaling-downscaling" scheme, as described by Dong et al. (2020). Here, the first option was used, and the 250 m DLST was compared with seven independent ALSTs (Table 1) that were not used in the model development. These seven representative dates demonstrate a high correlation between the MODIS and ASTER LST (correlation coefficient (R) greater than 0.9; see Supplementary Table A1).

ASTER and MODIS LSTs on the same dates might be dissimilar because of different sensor characteristics and retrieval algorithms (Hutengs and Vohland, 2016). To mitigate these incosistencies, this study modeled the linear relationship between the 1 km aggregated ASTER LST and MODIS LST (i.e., $LST_{MODIS} = a * LST_{ASTER} + b$) for each date. The obtained coefficients (see Supplementary Table A1) were then applied to the 250 m ASTER LST. The bias-corrected independent ALSTs were then used as reference data in the accuracy assessment. Four widely known metrics, such as R, root mean square error (RMSE), relative RMSE (rRMSE; ratio of RMSE to the standard deviation of the observed values) and mean absolute error (MAE) were calculated to compare each scheme's downscaling performance using bias-corrected reference ALSTs.

Table 1
The list of reference dates for ASTER land surface temperature (ALST) used for validation.

City	Reference date
Rome	8 October 2019, 6 July 2020, and 16 August 2020
Madrid	8 October 2017, 20 December 2017, and 21 June 2018
Seoul	18 March 2017

In addition to independent ALSTs, air temperatures were also used to evaluate the DLST data. This evaluation is predicated on the assumption that nighttime air temperatures and LST exhibit generally similar spatial patterns (Yoo et al., 2018), when the surface radiation budget is reduced to longwave fluxes only. To perform this evaluation, the LST products (i.e., DLST for each scheme, MODIS LST, and bias-corrected ALST) employed in this work were compared with in-situ air temperatures for seven reference dates and the spatial correlation coefficient (R) was calculated.

3.3. Deriving mean annual surface temperature and SUHI analysis

Based on the evaluation of the three schemes, the best-performing scheme was then used to downscale all clear-sky (<1% cloud percentage) 1 km nighttime MODIS LSTs during the study period (2017–2020) to 250 m resolution. To identify thermal surface characteristics under largely cloud-free conditions and compare the LST patterns at various spatial scales, annual temperature cycle parameters (ACP) have been effectively used (Bechtel, 2015). The mean annual surface temperature (MAST), which is one component of ACP, was estimated for the 1 km MODIS LSTs and 250 m DLSTs for each year, based on the annual temperature cycle model (Supplementary Equation A1). The analysis of LST distribution was performed for the three cities through the constructed MASTs with different spatial resolutions (i.e., 1 km and 250 m).

In addition, we compared the nocturnal SUHI intensity between the constructed 1 km and 250 m MASTs using the LCZ map of each city. Based on the previous SUHI studies, LCZD (featureless landscapes of low plants) was selected as a reference class of natural-type LCZ (Bechtel et al., 2019). Only the LCZ classes, which accounted for more than 1% of the entire study area in each city, were used for this analysis. The SUHI intensity for each LCZ class was calculated using equation (1):

$$SUHI_{LCZX} = LST_{LCZX} - LST_{LCZD} \quad (1)$$

where LST_{LCZX} is the mean MAST value for LCZX (e.g., LCZ1 and LCZ2). Because the LCZ map has a 250 m spatial resolution, the 1 km MAST was resampled to 250 m with a nearest neighbor before calculating the SUHI intensity.

3.4. Temporal correlation analysis between daily DLSTs and nighttime in-situ air temperatures

In general, LST and air temperature show a high temporal correlation at nighttime (Tomlinson et al., 2012). We further tested whether the degree of this correlation varies according to the spatial resolution (i.e., 250 m and 1 km) of LST. At each weather station, the temporal correlation (R) between the nighttime air temperature and the LST value of the grid (where the station is located) was individually calculated for 250 m DLSTs and 1 km MODIS LSTs. Here all clear-sky LSTs during the study period were used in the calculation.

4. Results and discussion

4.1. LST downscaling evaluation

The validation results based on reference ALST data are presented in Figs. 3–5 for Rome, Madrid, and Seoul, respectively. Compared to S1, S2 using the selected ALSTs as input kernels showed a distinct increase in performance for all validation dates. In particular, the R-value of S2 was close to 0.93 for all three cities. The RMSE and MAE of S2 also

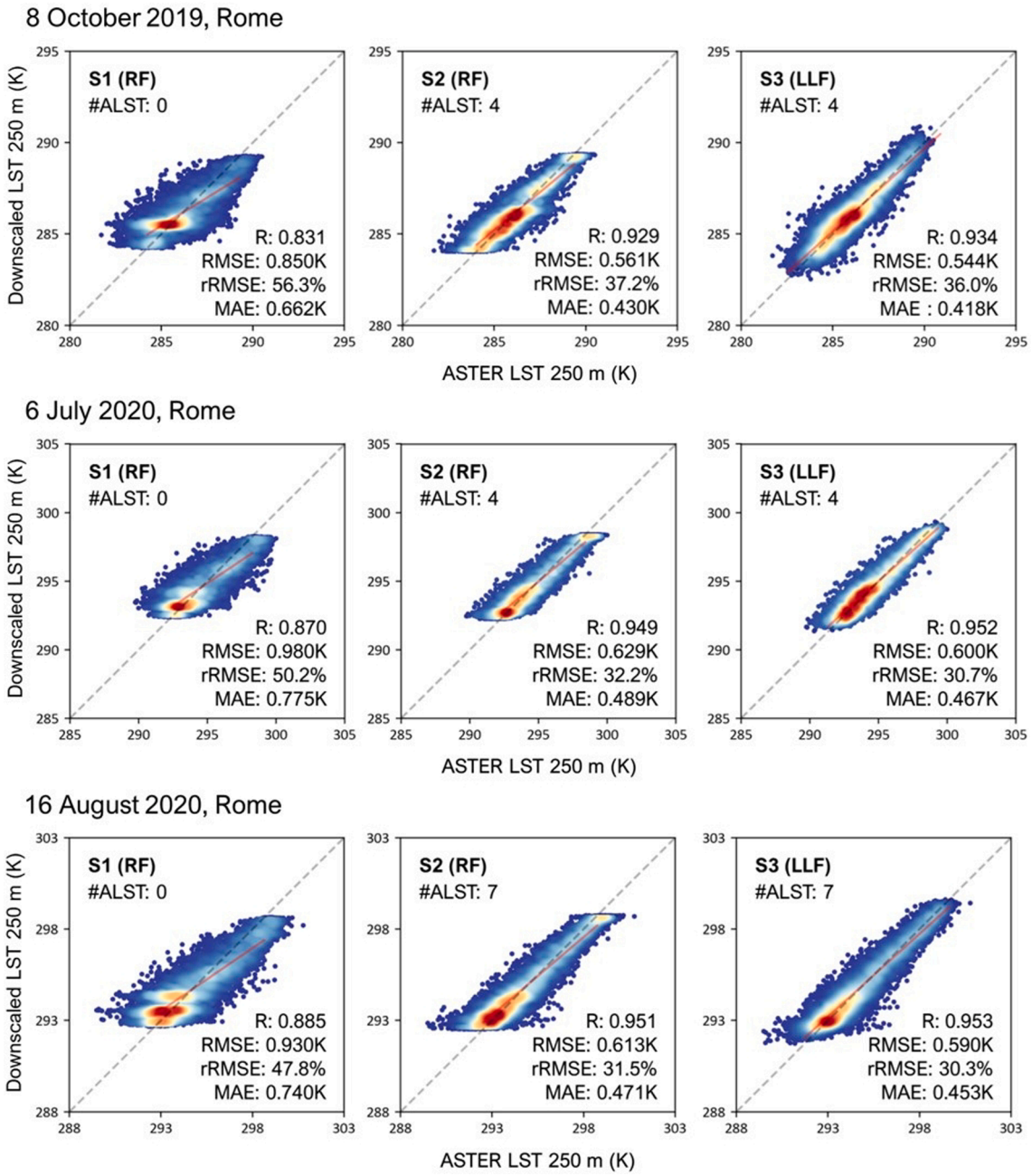

Fig. 3. Scatterplots of the downscaled and bias-corrected ASTER reference LST of three schemes for the validation dates in Rome. The increasing density of the paired samples is indicated by a color scheme ranging from blue to red. The regression line is represented by red solid lines and the identity line by grey dashed lines; #ALST is the number of ALST selected as input kernels.

significantly decreased (about 0.32 K and 0.25 K, respectively) compared to S1, where the RMSE of S2 was less than 1 K for all dates. Notably, S2 was better at predicting high LSTs than S1 was, considering that the predictions of S2 are densely concentrated near the identity line (i.e., y = x) for high values. In general, high LSTs appear in dense impervious surfaces in a city (Yuan and Bauer, 2007). Therefore, S2 better captures the SUHI phenomena, which is a thermal difference between the urban and the surrounding areas. Qi et al. (2020) used the Landsat daytime reflectance and the thermal infrared data as input kernels to downscale nighttime LSTs. Nighttime LST, however, shows a different spatial pattern from that of daytime, especially in urban landscapes (Zhao et al., 2017). The results of S2 suggest that it is essential to use input kernels that can effectively represent the nocturnal thermal patterns in downscaling the nighttime LST.

S3 showed the best performance among the three schemes for all dates in the three cities (Figs. 3–5). Compared to the prediction of S3, those of S1 and S2 were concentrated near specific upper and lower values (i.e., narrow dynamic ranges). This is because RF predicts the values within the trained coverage to minimize the mean squared error. Interestingly, LLF-based S3 predicted LST with high linearity, especially for both extremes, much better than S2. The effect of the local linear adjustment in LLF using the selected ALST kernels was evident in the S3 results. The S3 performance with the average R of 0.94, RMSE of 0.64 K, and MAE of 0.50 K for the three cities is much better than those of the previous studies which tried to downscale nighttime LST. Qi et al. (2020), for example, downscaled the MODIS nighttime LST to 100 m resolution for Suzhou, China, resulting in R of 0.90, RMSE of 1.76 K and MAE is 1.48 K. Wang et al. (2020a) produced 30 m resolution nighttime

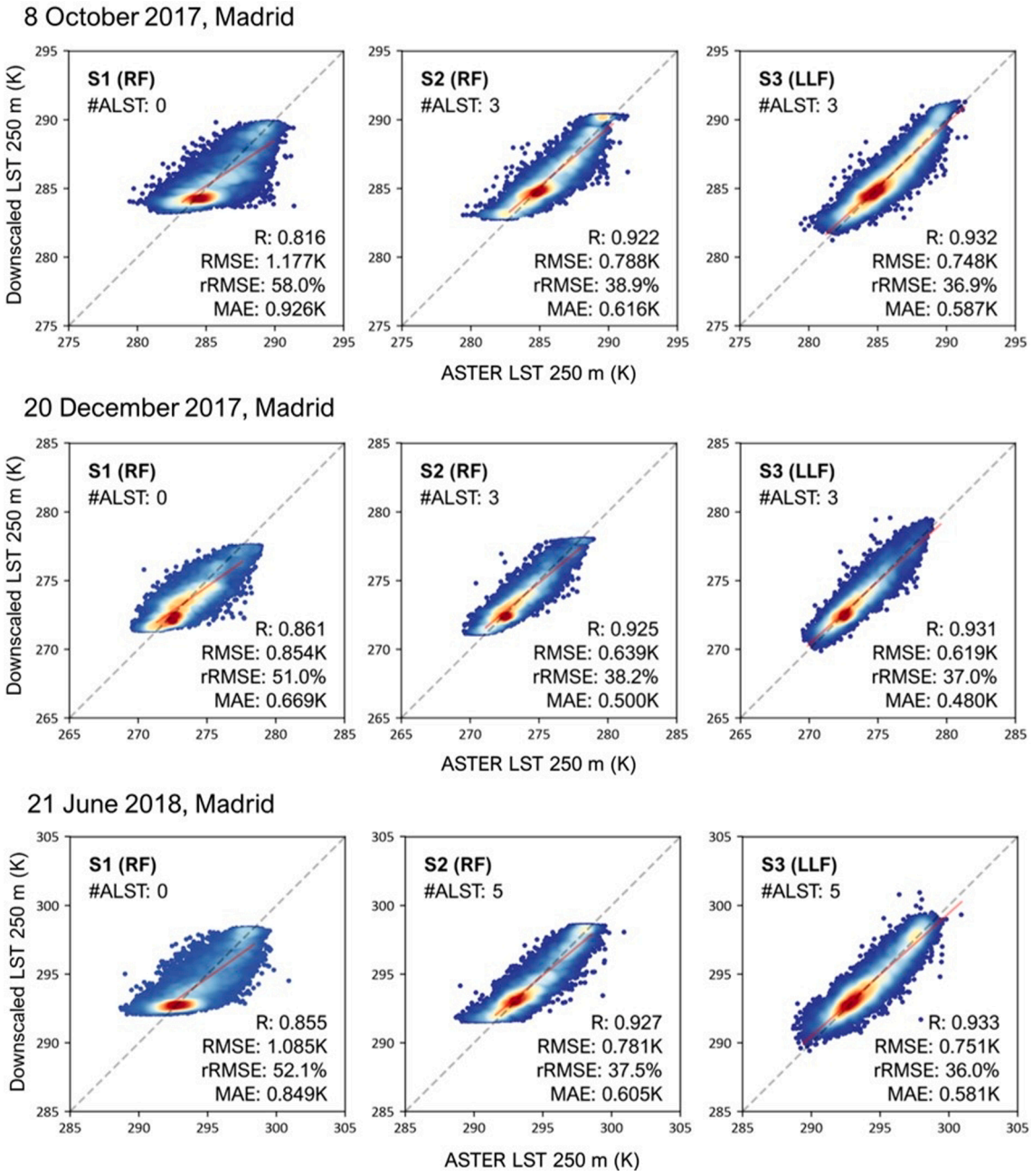

Fig. 4. Same as Fig. 3 but for Madrid.

LST from MODIS LST for the subregion of Singapore, with a performance of RMSE of 3.50 K and MAE of 2.81 K. Although the study area and target spatial resolutions are different among the studies, the suggested S3 proved to show excellent downscaling performance. In particular, the proposed S3 showed high linearity for both extremes resulting in slopes ~ 1 and low biases for all three cities.

Fig. 6 shows the spatial distribution of DLSTs of reference ALSTs and three schemes (S1–S3) for one validation date. Overall, all three schemes showed obvious urban–rural LST gradients where the high LSTs appear near the city center and become lower toward the periphery. The gradient of S1, however, appears relatively smooth compared to those of S2 and S3. Moreover, some regions in S1 could not effectively predict the temperature pattern, such as areas bounded by the black box in each city.

Remarkably, the DLST of S2 and S3 also showed different spatial patterns. For example, S2 tended to predict the temperature as lower than the reference ALST for regions with dense buildings (LCZ1-3 areas in Fig. 1) in the three cities. S2 also failed to predict LST accurately for regions where the temperature should appear lower than the predicted values (e.g., the surrounding rural regions bounded by a black box). The reduced dynamic ranges at the downscaled LST using a tree-based model also appear in the existing study (Qi et al., 2020). On the other hand, S3 showed a relatively similar LST distribution with reference ALST, compared to S2.

The spatial distribution of the bias for the three schemes is depicted in Fig. 7, along with their error frequency for the extreme LST values. S1 had a wide error distribution where large positive and negative biases appeared for urban and natural type surfaces, respectively, for the three cities. Bias distribution for both S2 and S3 showed a relatively narrow range compared to that of S1. While no distinct bias differences between S2 and S3 were found in overall spatial distribution, S3 had the highest frequency of near-zero error for the extreme LST values (see right

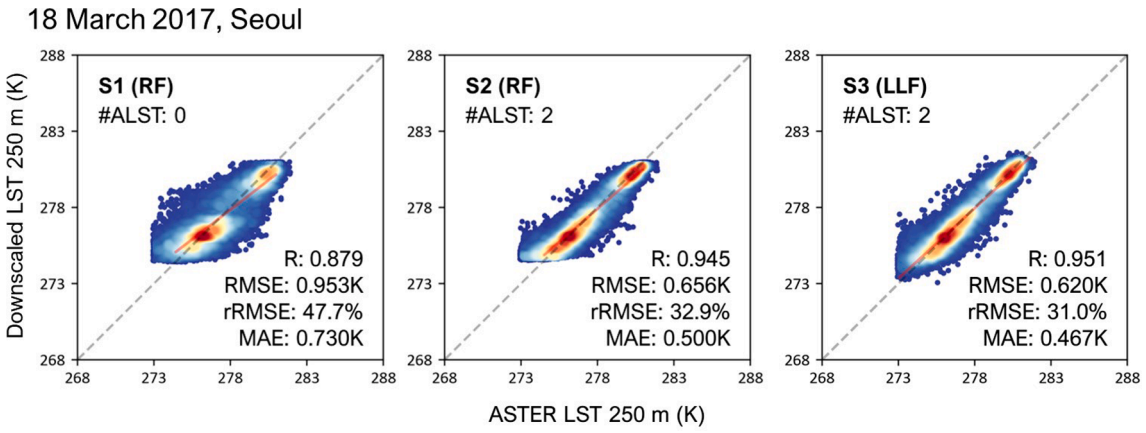

Fig. 5. Same as Fig. 3 but for Seoul.

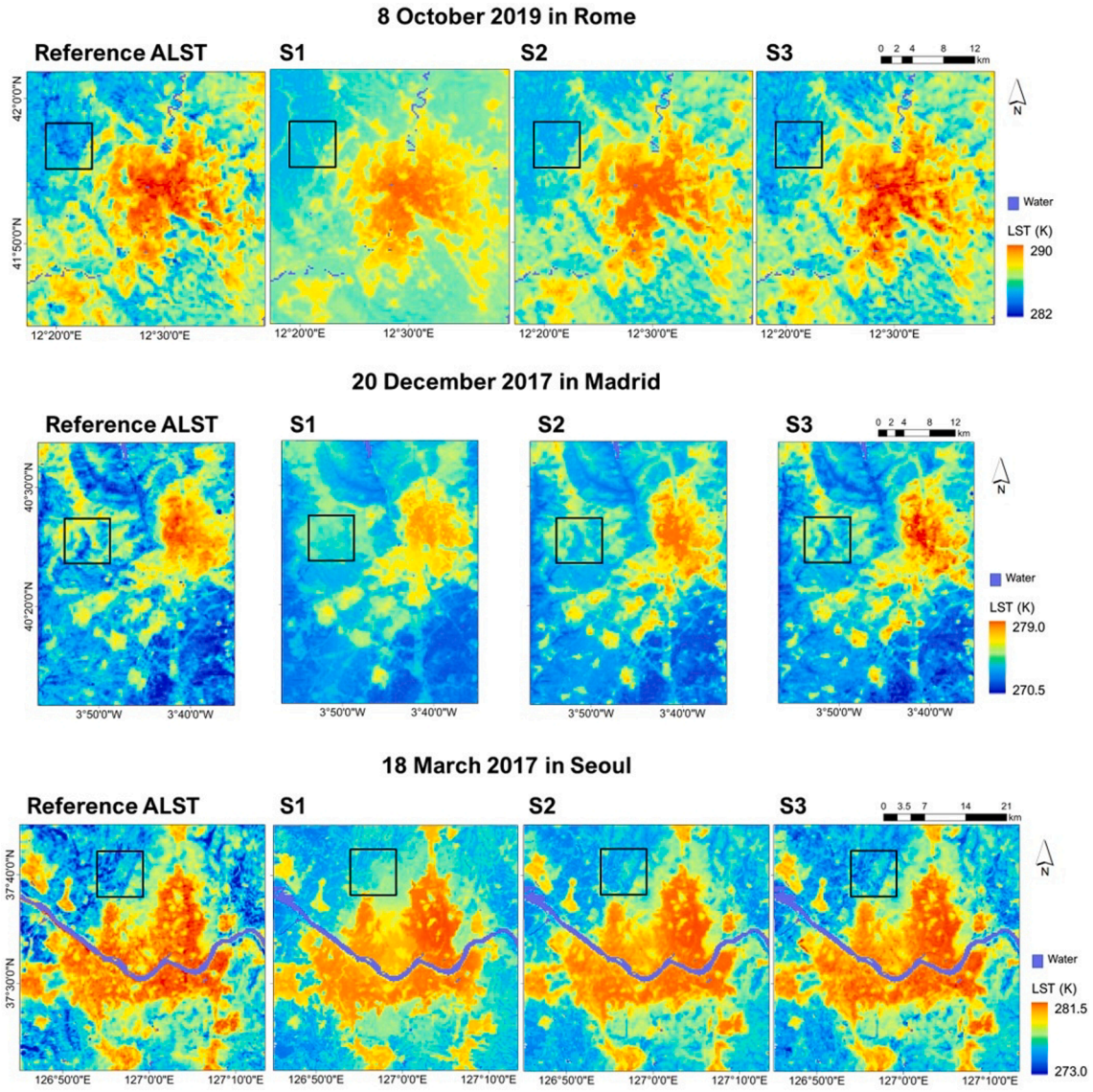

Fig. 6. Spatial distribution of nighttime LST on 8 October 2019 in Rome, 20 December 2017 in Madrid, and 18 March 2017 in Seoul. The maps of the bias-corrected reference ALST and downscaled LSTs for scheme 1 (S1), scheme 2 (S2), and scheme 3 (S3) are shown.

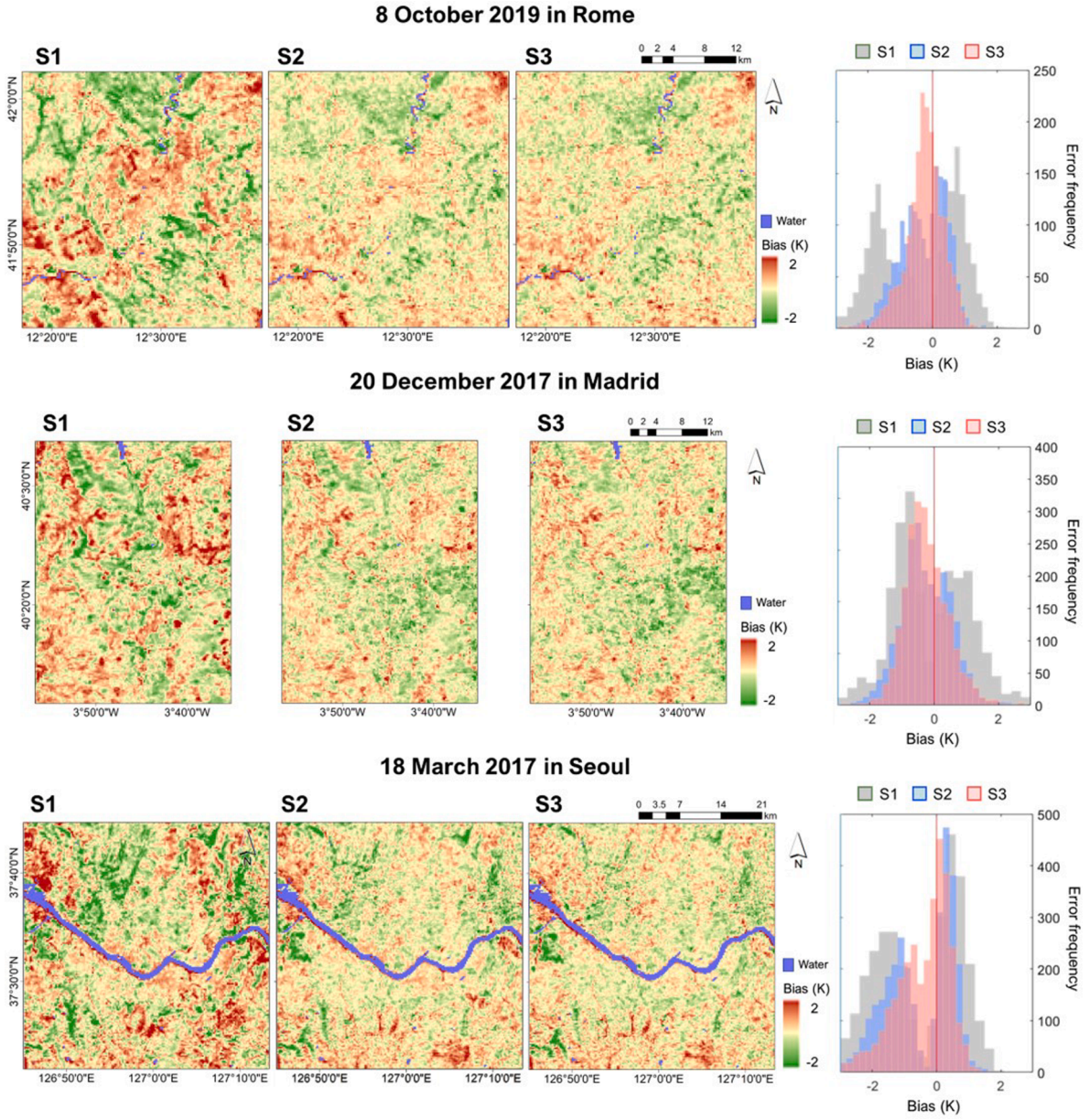

Fig. 7. Spatial distribution of the bias of schemes 1–3 (S1-S3) and error frequency diagrams for extreme values (right) for dates corresponding to Fig. 6. Bias was the difference between the bias-corrected reference ALST and DLST for each scheme. Extreme LSTs were defined as those with values below 5th percentile or above the 95th percentile for each study area.

diagrams in Fig. 7). These results agree with Figs. 3–5, in which S3 using the LLF model can predict the extremely low and high LST values better than S2.

The number of the selected ALSTs used in the models varied by the validation dates (Figs. 3–5). We further tested S2 and S3 when only one among the selected ALSTs was used for each validation date. Supplementary Table A2 presents the S2 and S3 performance when one of the selected ALSTs was used. Even when only one ALST was used, S2 showed higher accuracy for all validation dates compared to S1 (See Figs. 3–5). This suggests that S2 could meaningfully improve the S1 performance, even when using one ALST as an input kernel. Moreover, S3 still showed the highest performance among the three schemes. The linear adjustment used in the LLF model proved effective even for using just one ALST as an input kernel. It is not surprising that S2 and S3 in Supplementary Table A2 using one ALST showed lower performance than those of S2 and S3 using all available ALSTs as input kernels. This implies that as the number of selected ALSTs increases, the accuracy of S2 and S3 is likely to improve.

Several previous kernel-driven downscaling studies, particularly for the daytime LST, used residual corrections to the DLSTs produced by machine learning models (Yang et al., 2017; Wang et al., 2020b; Bartkowiak et al., 2019). Supplementary Table A3 shows the downscaling accuracy for the validation datasets using the residual correction method suggested by Hutengs and Vohland (2016). After residual correction, the S1 performance improved, which is consistent with the results of Hutengs and Vohland (2016) that used MODIS reflectance kernels to downscale daytime LSTs. In most validation dates, however, the S2 and S3 performance deteriorated after residual correction (see Supplementary Table A3 and Figs. 4–6). One possible explanation is that the residual correction method assumes invariance of the residual terms (i.e., the difference between aggregated DLST and original MODIS LST) within the local region (Liu et al., 2020). However, this assumption may be inappropriate in heterogeneous landscapes, such as urban areas, where the downscaling performance is already sufficiently good prior to

Table 2
The spatial correlation (R) between each LST product (MODIS LST, bias-corrected ALST, and the three schemes' DLSTs) and in-situ nighttime air temperature for seven reference dates.

Rome	MODIS	ALST	S1	S2	S3
8 October 2019	0.543	0.616	0.574	0.616	0.618
6 July 2020	0.539	0.654	0.495	0.570	0.579
16 August 2020	0.611	0.643	0.557	0.633	0.639
Madrid	**MODIS**	**ALST**	**S1**	**S2**	**S3**
8 October 2017	0.491	0.679	0.470	0.661	0.687
20 December 2017	0.407	0.563	0.357	0.512	0.522
21 June 2018	0.766	0.777	0.526	0.721	0.723
Seoul	**MODIS**	**ALST**	**S1**	**S2**	**S3**
18 March 2017	0.703	0.818	0.713	0.828	0.831

residual correction. The S2 and S3 that used the selected ALSTs as input kernels were able to produce reasonably accurate nighttime DLSTs in urban areas without additional residual correction.

Table 2 shows the spatial correlation between each LST product and nighttime *in-situ* air temperatures for the seven reference dates. ALST has a higher correlation with air temperature than MODIS LST does for all reference dates. This implies that fine resolution LSTs exhibit spatial patterns more similar to those of air temperature in urban areas. S2 and S3 exhibit significantly superior spatial performance to S1 in all cases, which corresponds to the validation results based on the reference ALST shown in Figs. 3–5. S3 demonstrates a slightly higher correlation with air temperature than S2, producing comparable results with ALST.

4.2. Applicability of the proposed method

4.2.1. Producing DLSTs for multiple dates

At least one ALST was selected on more than 95% of the days in all

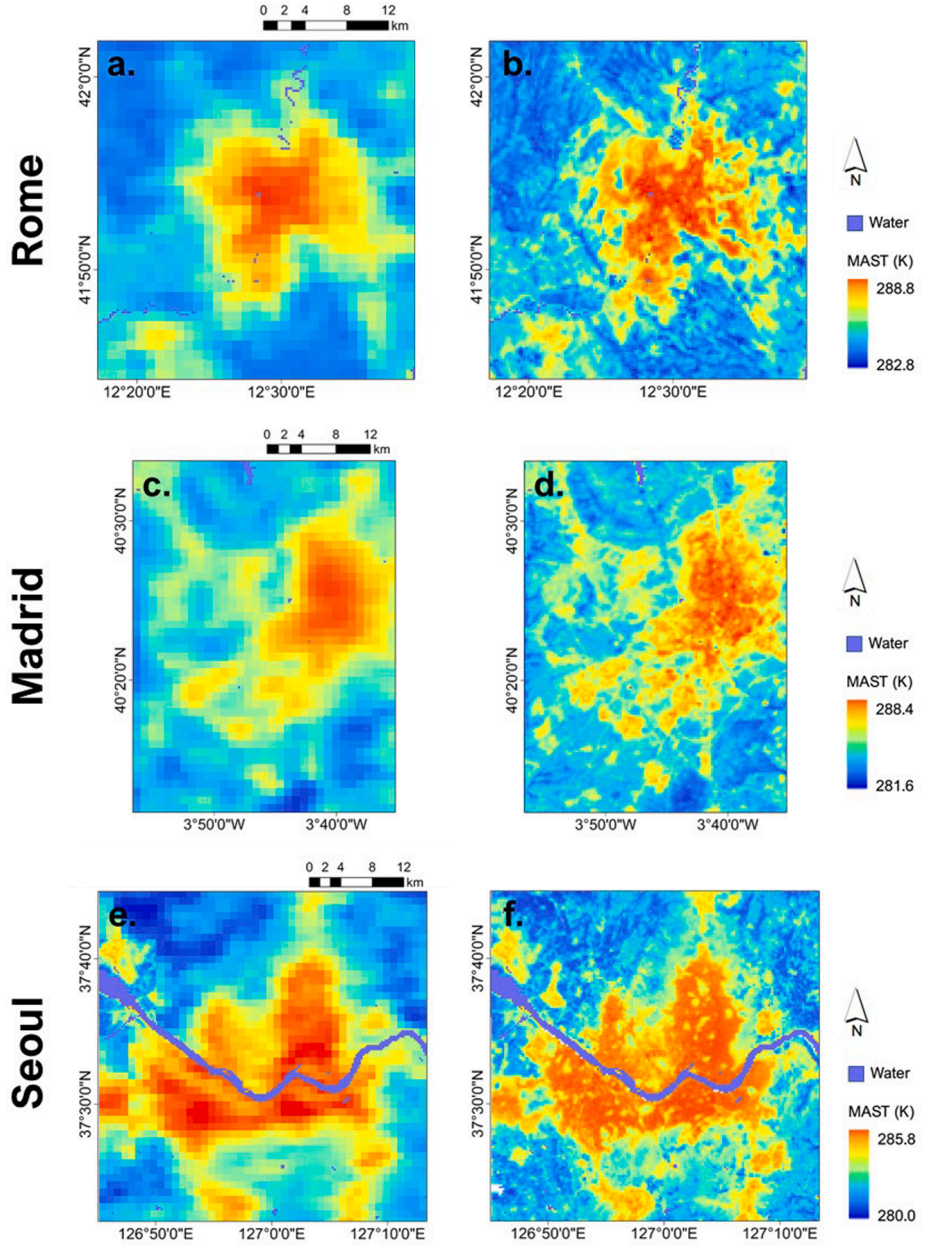

Fig. 8. Spatial distribution of four-year average nighttime MAST from 1 km MODIS LSTs (a, c, e) and 250 m DLSTs based on scheme 3 (b, d, f) for the three cities. DLSTs in S3 were generated only for the dates when at least one ALST was selected by LASSO.

three cities by LASSO for the clear-sky nighttime MODIS LSTs from 2017 to 2020 (Supplementary Table A4). When there were many available ALSTs in Rome, three or more ALSTs were selected on about 60% of the days. In general, the temporal changes of spatial distribution for the nighttime LSTs appeared quite stable in urban areas (Hu and Brunsell, 2013). The ALST selection method suggested in this study proved to be suitable for downscaling nighttime LST for multiple dates.

Fig. 8 shows the four-year average MAST calculated using clear-sky daily nighttime MODIS LST and S3-based DLST from 2017 to 2020. In both 1 km and 250 m MAST for all three cities, higher LST appeared in urban core areas, while the urban periphery had relatively lower LST. The 250 m MAST, however, showed the LST distribution in greater detail than the 1 km MAST. In particular, some built-up regions, including urban centers and suburban clusters, showed distinctively high LST in the 250 m data. This implies that the fine-resolution LST (i.e., DLST) could help extract local hot spots more precisely in cities than the LSTs with relatively coarse resolution (Sidiqui et al., 2016).

4.2.2. Applicability for urban climate monitoring

Table 3 shows the SUHI intensity for each LCZ calculated from 1 km and 250 m MASTs, respectively. Positive SUHI appeared in the built types (LCZ2-6 and 8) for all three cities in both 1 km and 250 m MASTs. Notably, compact types (LCZ2 and 3) showed stronger intensity than open types (LCZ4-6). This finding is consistent with the results of the previous studies that nocturnal SUHI intensity demonstrates a high correlation with building compactness (Dian et al., 2020; Bechtel et al., 2019). Compared to 1 km, 250 m MAST showed larger SUHI for most built type LCZs, and smaller SUHI for natural type LCZs. This implies that various urban and natural structures are mixed within coarse grids (i.e., MODIS 1 km), resulting in the underestimation of the SUHI intensity of the built-type surfaces (Bechtel et al., 2019).

Table 4 shows the average temporal correlation between nighttime LST and air temperature for the 1 km MODIS LST and 250 m DLST. The 250 m DLST showed a higher temporal correlation with the nighttime air temperature than the MODIS 1 km LST. The 250 m DLST shows a relatively similar temporal pattern with air temperature, even for periods with relatively small temperature change (i.e., DJF and JJA).

4.3. Novelty and limitations

This is the first study that we are aware of that utilizes LLF to downscale LST. The proposed approach is novel in that it uses as input kernels feature-selected ALSTs of other dates that have a spatial distribution similar to the target date LST. The ALST kernels were important in maintaining the dynamic range of the original LST by acting as linear adjusted variables in the LLF model. The proposed method was evaluated for three cities, each with its own distinct geographic and climatic characteristics. Many previous LST downscaling studies—mostly for the daytime LST—used a single city as the study area (Yang et al., 2017; Qi et al., 2020; Wang et al., 2020a), and conducted accuracy assessment using data for a small number of dates (i.e., only one day; Yang et al., 2017; Qi et al., 2020), limiting the generalization of their methods. The validity of the proposed downscaling method was established through testing on multiple dates in three cities with varying characteristics. This study is also significant because it demonstrated the broad applications of the DLSTs—UHI intensity analysis and air temperature monitoring at nighttime in urban areas.

A major limitation of this study is that the method relies heavily on the availability of ALSTs. There are many cloudless ALSTs in cities with dry climates such as Rome and Madrid, but only a few clear-sky ALSTs in humid cities such as Seoul. Cloud gap-filling algorithms, particularly for MODIS LST, have been recently developed (Zhao and Duan, 2020; Zhang et al., 2021; Cho et al., 2022). If these techniques are applied to high-resolution LST such as ASTER LST, it is expected that gap-filled LST can be used as input. In addition, a number of fine-resolution thermal data have become available, such as those collected by the ECOsystem Spaceborne Thermal Radiometer Experiment on Space Station (ECOSTRESS). While these thermal data have the acquisition times different from the MODIS LST, they could be considered candidates for ALST input kernels. Auxiliary input kernels also introduce some limitations. The uncertainty inherent in each input kernel affects the downscaling accuracy. For example, the wind kernel, a ten-year average wind speed containing long-term climate characteristics, may not accurately represent the wind field characteristics of cities for the target study period. In addition, uncertainty in the DEM and slope kernels might increase when fine resolution (i.e., 90 m) data were aggregated to 250 m.

5. Conclusion

This study presents a new nighttime LST downscaling method in which 250 m DLST is generated from 1 km MODIS nighttime LST in Rome, Madrid, and Seoul. We developed and compared three downscaling schemes (S1-S3). When comparing the three schemes using the

Table 4
Temporal correlation coefficients (R values) between daily clear-sky LSTs and nighttime air temperatures for four different seasons (i.e., December to February—DJF, March to May—MAM, June to August—JJA, September to November—SON) for the three cities. One (1) km and 250 m represent the LSTs of the 1 km MODIS LSTs and scheme 3-based DLSTs, respectively.

	Rome		Madrid		Seoul	
Season	1 km	250 m	1 km	250 m	1 km	250 m
DJF	0.882	0.890	0.912	0.923	0.944	0.954
MAM	0.943	0.949	0.961	0.969	0.964	0.964
JJA	0.725	0.728	0.742	0.759	0.747	0.759
SON	0.982	0.984	0.980	0.984	0.978	0.978
Average	0.883	0.888	0.899	0.909	0.908	0.914

Table 3
SUHI intensity of each LCZ class based on four-year average MAST from MODIS LSTs (1 km) and scheme 3-based DLSTs (250 m) for the three cities. Diff implies the difference between the intensity of 250 m and 1 km MAST for each LCZ class. The unit of SUHI intensity is Kelvin (K).

SUHI	Rome			Madrid			Seoul		
LCZ	1 km	250 m	diff	1 km	250 m	diff	1 km	250 m	diff
2	3.04	3.53	0.49	2.61	2.89	0.28	3.14	3.27	0.13
3							2.74	2.87	0.14
4							2.24	2.42	0.18
5	1.56	1.84	0.27	1.93	2.36	0.44	1.65	1.68	0.03
6	0.65	0.69	0.04	0.86	1.10	0.24	1.18	1.15	−0.03
8	1.10	1.35	0.25	1.04	1.16	0.12	1.12	1.17	0.05
A	0.82	0.79	−0.03				0.59	0.56	−0.03
B	0.17	0.11	−0.06	0.01	0.00	−0.01	0.39	0.35	−0.04
C				0.06	−0.03	−0.09			

bias-corrected ALSTs for seven reference dates, S3, the best performing scheme, yielded very promising results, with R ~ 0.94 and RMSE ~ 0.64 K for all three cities. S3, which used the selected ALSTs and eight auxiliary input kernels: NDVI, DEM, Slope, DisBWC, Road, Pop, Built-up, and Wind through the LLF model, predicted LST much better than other schemes, especially for both extremes. The S3-based DLST showed relatively accurate and reasonable spatial distribution, resulting in distinct urban–rural nocturnal thermal gradients. S3-based DLST showed larger SUHI intensity on urban surfaces and a higher temporal correlation with nighttime air temperature than 1 km MODIS LST did. This study revealed that the LLF machine learning model could improve the downscaling accuracy, compared to RF, by using the selected ALST as linear adjustment kernels to maintain the dynamic range of the original LST. We believe that the proposed approach can be successfully applied to other global cities and that it will help us see the nocturnal SUHI phenomena in various aspects, such as different types of urban forms.

CRediT authorship contribution statement

Cheolhee Yoo: Conceptualization, Methodology, Validation, Formal analysis, Visualization, Writing – original draft, Writing – review & editing. **Jungho Im:** Methodology, Supervision, Writing – review & editing, Funding acquisition. **Dongjin Cho:** Methodology, Writing – review & editing. **Yeonsu Lee:** Writing – review & editing. **Dukwon Bae:** Writing – review & editing. **Panagiotis Sismanidis:** Writing – review & editing.

Declaration of Competing Interest

The authors declare that they have no known competing financial interests or personal relationships that could have appeared to influence the work reported in this paper.

Acknowledgements

This research was supported by the Korea Meteorological Administration Research and Development Program under Grant KMIPA 2017–7010, by the National Research Foundation of Korea under Grant NRF-2021R1A2C2008561, and by Korea Ministry of Environment (MOE) (2021003330001 (NTIS: 1485017948)). CY was partially supported by Global PhD Fellowship Program through the National Research Foundation of Korea (NRF-2018H1A2A1062207).

Appendix A. Supplementary material

Supplementary data to this article can be found online at https://doi.org/10.1016/j.jag.2022.102827.

References

Abdollahipour, A., Ahmadi, H., Aminnejad, B., 2022. A review of downscaling methods of satellite-based precipitation estimates. Earth Sci. Inf. 15 (1), 1–20.
Alexander, C., 2020. Normalised difference spectral indices and urban land cover as indicators of land surface temperature (LST). Int. J. Appl. Earth Obs. Geoinf. 86, 102013. https://doi.org/10.1016/j.jag.2019.102013.
Azevedo, J., Chapman, L., Muller, C., 2016. Quantifying the daytime and night-time urban heat island in Birmingham, UK: A comparison of satellite derived land surface temperature and high resolution air temperature observations. Remote Sens. 8 (2), 153. https://doi.org/10.3390/rs8020153.
Bartkowiak, P., Castelli, M., Notarnicola, C., 2019. Downscaling land surface temperature from MODIS dataset with random forest approach over alpine vegetated areas. Remote Sens. 11 (11), 1319. https://doi.org/10.3390/rs11111319.
Bechtel, B., 2015. A new global climatology of annual land surface temperature. Remote Sens. 7 (3), 2850–2870.
Bechtel, B., Demuzere, M., Mills, G., Zhan, W., Sismanidis, P., Small, C., Voogt, J., 2019. SUHI analysis using Local Climate Zones—A comparison of 50 cities. Urban Clim. 28, 100451. https://doi.org/10.1016/j.uclim.2019.01.005.
Breiman, L., 2001. Random forests. Mach. Learn. 45, 5–32.
Cho, D., Bae, D., Yoo, C., Im, J., Lee, Y., Lee, S., 2022. All-Sky 1 km MODIS Land Surface Temperature Reconstruction Considering Cloud Effects Based on Machine Learning. Remote Sens. 14 (8), 1815. https://doi.org/10.3390/rs14081815.
Dian, C., Pongrácz, R., Dezső, Z., Bartholy, J., 2020. Annual and monthly analysis of surface urban heat island intensity with respect to the local climate zones in Budapest. Urban Clim. 31, 100573. https://doi.org/10.1016/j.uclim.2019.100573.
Dong, P., Gao, L., Zhan, W., Liu, Z., Li, J., Lai, J., Li, H., Huang, F., Tamang, S.K., Zhao, L., 2020. Global comparison of diverse scaling factors and regression models for downscaling Landsat-8 thermal data. ISPRS J. Photogramm. Remote Sens. 169, 44–56.
Duan, S.-B., Li, Z.-L., 2016. Spatial downscaling of MODIS land surface temperatures using geographically weighted regression: Case study in northern China. IEEE Trans. Geosci. Remote Sens. 54 (11), 6458–6469.
Duan, S.-B., Li, Z.-L., Cheng, J., Leng, P., 2017. Cross-satellite comparison of operational land surface temperature products derived from MODIS and ASTER data over bare soil surfaces. ISPRS J. Photogramm. Remote Sens. 126, 1–10.
Duan, S.-B., Li, Z.-L., Li, H., Göttsche, F.-M., Wu, H., Zhao, W., Leng, P., Zhang, X., Coll, C., 2019. Validation of Collection 6 MODIS land surface temperature product using in situ measurements. Remote Sens. Environ. 225, 16–29.
Ebrahimy, H., Azadbakht, M., 2019. Downscaling MODIS land surface temperature over a heterogeneous area: An investigation of machine learning techniques, feature selection, and impacts of mixed pixels. Comput. Geosci. 124, 93–102.
Friedberg, R., Tibshirani, J., Athey, S., Wager, S., 2021. Local linear forests. J. Comput. Graph. Stat. 30 (2), 503–517.
Gillespie, A., Rokugawa, S., Matsunaga, T., Cothern, J.S., Hook, S., Kahle, A.B., 1998. A temperature and emissivity separation algorithm for Advanced Spaceborne Thermal Emission and Reflection Radiometer (ASTER) images. IEEE Trans. Geosci. Remote Sens. 36 (4), 1113–1126.
Hu, L., Brunsell, N.A., 2013. The impact of temporal aggregation of land surface temperature data for surface urban heat island (SUHI) monitoring. Remote Sens. Environ. 134, 162–174.
Hutengs, C., Vohland, M., 2016. Downscaling land surface temperatures at regional scales with random forest regression. Remote Sens. Environ. 178, 127–141.
Li, W., Ni, L.i., Li, Z.-L., Duan, S.-B., Wu, H., 2019. Evaluation of machine learning algorithms in spatial downscaling of MODIS land surface temperature. IEEE J. Sel. Top. Appl. Earth Obs. Remote Sens. 12 (7), 2299–2307.
Liao, W., Liu, X., Wang, D., Sheng, Y., 2017. The impact of energy consumption on the surface urban heat island in China's 32 major cities. Remote Sens. 9 (3), 250. https://doi.org/10.3390/rs9030250.
Liu, K., Su, H., Li, X., Chen, S., 2020. Development of a 250-m Downscaled Land Surface Temperature Data Set and Its Application to Improving Remotely Sensed Evapotranspiration Over Large Landscapes in Northern China. IEEE Trans. Geosci. Remote Sens.
Luo, X., Chen, Y., Wang, Z., Li, H., Peng, Y., 2021. Spatial Downscaling of MODIS Land Surface Temperature Based on a Geographically and Temporally Weighted Autoregressive Model. IEEE J. Sel. Top. Appl. Earth Obs. Remote Sens. 14, 7637–7653.
Mallick, J., Rahman, A., Singh, C.K., 2013. Modeling urban heat islands in heterogeneous land surface and its correlation with impervious surface area by using night-time ASTER satellite data in highly urbanizing city, Delhi-India. Adv. Space Res. 52, 639–655.
Odebiri, O., Mutanga, O., Odindi, J., Peerbhay, K., Dovey, S., 2020. Predicting soil organic carbon stocks under commercial forest plantations in KwaZulu-Natal province, South Africa using remotely sensed data. GISci. Remote Sens. 57, 450–463.
Pan, X., Zhu, X., Yang, Y., Cao, C., Zhang, X., Shan, L., 2018. Applicability of downscaling land surface temperature by using normalized difference sand index. Sci. Rep. 8, 1–14.
Peng, J., Loew, A., Merlin, O., Verhoest, N.E., 2017. A review of spatial downscaling of satellite remotely sensed soil moisture. Rev. Geophys. 55, 341–366.
Peng, Y., Li, W., Luo, X., Li, H., 2019. A geographically and temporally weighted regression model for spatial downscaling of MODIS land surface temperatures over urban heterogeneous regions. IEEE Trans. Geosci. Remote Sens. 57, 5012–5027.
Qi, P., Cui, Y., Zhang, H., Hu, S., Yao, L., Li, L.B., 2020. Evaluating Multivariable Statistical Methods for Downscaling Nighttime Land Surface Temperature in Urban Areas. IEEE Access 8, 162085–162098.
Sahoo, S., Gupta, P., Srivastav, S., 2020. Inter-calibration of DMSP-OLS and SNPP-VIIRS-DNB annual nighttime light composites using machine learning. GISci. Remote Sens. 57, 1144–1165.
Sidiqui, P., Huete, A., Devadas, R., 2016. Spatio-temporal mapping and monitoring of Urban Heat Island patterns over Sydney, Australia using MODIS and Landsat-8, 2016 4th International Workshop on Earth Observation and Remote Sensing Applications (EORSA). IEEE 217–221.
Sismanidis, P., Bechtel, B., Keramitsoglou, I., Göttsche, F., Kiranoudis, C.T., 2021. Satellite-derived quantification of the diurnal and annual dynamics of land surface temperature. Remote Sens. Environ. 265, 112642.
Stewart, I.D., Oke, T.R., 2012. Local climate zones for urban temperature studies. Bull. Am. Meteorol. Soc. 93, 1879–1900.
Tibshirani, R., 1996. Regression shrinkage and selection via the lasso. J. Roy. Stat. Soc.: Ser. B (Methodol.) 58, 267–288.
Tomlinson, C.J., Chapman, L., Thornes, J.E., Baker, C.J., Prieto-Lopez, T., 2012. Comparing night-time satellite land surface temperature from MODIS and ground measured air temperature across a conurbation. Remote Sens. Lett. 3, 657–666.
Tovar-Pescador, J., Pozo-Vázquez, D., Ruiz-Arias, J., Batlles, J., López, G., Bosch, J., 2006. On the use of the digital elevation model to estimate the solar radiation in areas of complex topography. Meteorol. Appl. 13, 279–287.

Wan, Z., Dozier, J., 1996. A generalized split-window algorithm for retrieving land-surface temperature from space. IEEE Trans. Geosci. Remote Sens. 34, 892–905.
Wang, J.W., Chow, W.T., Wang, Y.-C., 2020a. A global regression method for thermal sharpening of urban land surface temperatures from MODIS and Landsat. Int. J. Remote Sens. 41, 2986–3009.
Wang, R., Gao, W., Peng, W., 2020b. Downscale MODIS land surface temperature based on three different models to analyze surface urban heat island: A case study of Hangzhou. Remote Sens. 12, 2134.
Weng, Q., Firozjaei, M., Sedighi, A., Kiavarz, M., Alavipanah, S., 2019. Statistical analysis of surface urban heat island intensity variations: A case study of Babol city. Iran. GISci. Remote Sens. 56, 576–604.
Xian, G., Shi, H., Auch, R., Gallo, K., Zhou, Q., Wu, Z., Kolian, M., 2021. The effects of urban land cover dynamics on urban heat island intensity and temporal trends. GISci. Remote Sens. 58, 501–515.
Yamamoto, Y., Ishikawa, H., 2018. Spatiotemporal variability characteristics of clear-sky land surface temperature in urban areas of Japan observed by Himawari-8. Sola.
Yang, C., Zhan, Q., Lv, Y., Liu, H., 2019. Downscaling land surface temperature using multiscale geographically weighted regression over heterogeneous landscapes in Wuhan, China. IEEE J. Sel. Top. Appl. Earth Obs. Remote Sens. 12, 5213–5222.
Yang, Y., Cao, C., Pan, X., Li, X., Zhu, X., 2017. Downscaling land surface temperature in an arid area by using multiple remote sensing indices with random forest regression. Remote Sens. 9, 789.
Yoo, C., Han, D., Im, J., Bechtel, B., 2019. Comparison between convolutional neural networks and random forest for local climate zone classification in mega urban areas using Landsat images. ISPRS J. Photogramm. Remote Sens. 157, 155–170.
Yoo, C., Im, J., Park, S., Cho, D., 2020a. Spatial Downscaling of MODIS Land Surface Temperature: Recent Research Trends, Challenges, and Future Directions. Korean J. Remote Sens. 36, 609–626.
Yoo, C., Im, J., Park, S., Quackenbush, L.J., 2018. Estimation of daily maximum and minimum air temperatures in urban landscapes using MODIS time series satellite data. ISPRS J. Photogramm. Remote Sens. 137, 149–162.
Yoo, C., Lee, Y., Cho, D., Im, J., Han, D., 2020b. Improving local climate zone classification using incomplete building data and Sentinel 2 images based on convolutional neural networks. Remote Sens. 12, 3552.
Yuan, F., Bauer, M.E., 2007. Comparison of impervious surface area and normalized difference vegetation index as indicators of surface urban heat island effects in Landsat imagery. Remote Sens. Environ. 106, 375–386.
Zhang, C., Long, D., Zhang, Y., Anderson, M.C., Kustas, W.P., Yang, Y., 2021. A decadal (2008–2017) daily evapotranspiration data set of 1 km spatial resolution and spatial completeness across the North China Plain using TSEB and data fusion. Remote Sens. Environ. 262, 112519.
Zhao, C., Jensen, J., Weng, Q., Currit, N., Weaver, R., 2020. Use of local climate zones to investigate surface urban heat islands in Texas. GISci. Remote Sens. 57, 1083–1101.
Zhao, G., Dong, J., Liu, J., Zhai, J., Cui, Y., He, T., Xiao, X., 2017. Different patterns in daytime and nighttime thermal effects of urbanization in Beijing-Tianjin-Hebei urban agglomeration. Remote Sens. 9, 121.
Zhao, W., Duan, S.-B., 2020. Reconstruction of daytime land surface temperatures under cloud-covered conditions using integrated MODIS/Terra land products and MSG geostationary satellite data. Remote Sens. Environ. 247.
Zhao, W., Wen, F., Wang, Q., Sanchez, N., Piles, M., 2021. Seamless downscaling of the ESA CCI soil moisture data at the daily scale with MODIS land products. J. Hydrol. 603.